

River incision, ^{10}Be production and transport in a source-to-sink sediment system (Var catchment, SW Alps)

Carole Petit¹, Tristan Salles², Vincent Godard^{3,4}, Yann Rolland^{5,6}, and Laurence Audin⁶

¹Université Côte d'Azur, CNRS, Observatoire de la Côte d'Azur, IRD, Géoazur, 250 rue Albert Einstein, Sophia Antipolis 06560 Valbonne, France

²School of Geosciences, The University of Sydney, Sydney, NSW 2006, Australia

³Aix-Marseille Université, CNRS, Coll France, IRD, INRAE, CEREGE, Aix en Provence, France

⁴Institut Universitaire de France (IUF), Paris, France

⁵EDYTEM, Université Savoie Mont Blanc, CNRS, UMR 5204, Le Bourget du Lac, France

⁶ISTerre, Université Grenoble Alpes, Univ. Savoie Mont Blanc, CNRS, IRD, IFSTTAR, 38000 Grenoble, France

Correspondence: Carole Petit (carole.petit@univ-cotedazur.fr)

Abstract. Detrital ^{10}Be from continental river sands or submarine sediments has been extensively used to determine the average long-term denudation rates of aerial catchments, based on the assumption that the rate of cosmnuclide production by interaction of source rocks with cosmic radiations balances out the loss of these elements by surface denudation. However, the ^{10}Be signal of produced sediments may be affected at the source by the response time of mountainous catchments to high frequency forcing; besides, transient sediment storage in piedmonts, alluvial plains, lakes or near the coast may also induce a difference between the erosive signal and its record in the sedimentary sink. Consequently, a significant part of the signal recorded in shallow-water sediments can be lost, as deep marine sediments may record simultaneously a signal coming from newly eroded source rocks along with one coming from the destabilization of previously deposited sediments.

In this paper, we use the Surface Process Model Badlands to simulate erosion, deposition and detrital ^{10}Be transfer from a source-to-sink sedimentary system (the Var River catchment, Southern French Alps) over the last 100 kyr. We first compare actual (i.e., model-based) denudation rates with the ones that would be extracted from the ^{10}Be record of local continental sediments (equivalent to river sands) and from off-shore deposited sediments over time, in order to examine if this record provides an accurate estimate of continental denudation rates. Then, we examine which conditions (precipitation rate, flexure, ice cover) permit to satisfy published measured river incision rates and ^{10}Be concentration in submarine sediments.

Our results, based on the Var catchment cosmic ray exposure dating and modelling indicate that, while river sands do accurately estimate the average denudation rate of continental catchments, it is much less the case for deep submarine sediments. We find that deep sea sediments have a different, and often much smoother ^{10}Be signature than continental ones, and record a significant time lag with respect to actual precipitation rate changes, representing the geomorphological response of the margin. A model which allows us to fit both measured ^{10}Be concentration in marine sediments and river incision rates on-land involves an increase in precipitation rates from 0.3 to 0.7 m.yr⁻¹ after 20 ka, suggesting more intense precipitations starting at the end of the Last Glacial Maximum.

1 Introduction

Sedimentary deposits are important archives of the tectonic and climatic history of continents: for instance, the geometry, grain size, mineralogy and geochemical signature of deposits are impacted by changes in environmental conditions (e.g., relative sea level changes and precipitations over geologic times, as well as human activities during the Anthropocene (Syvitski et al., 2022)). Provided good enough estimates of the transfer function between these sedimentary records and their external forcing, they can be reliable tools for reconstructing climatic cycles, subsidence curves, or monsoon onset for instance (Bentley et al., 2016; Li et al., 2016; Liu et al., 2016; Wan et al., 2006). However, depending on the considered timescales, the signatures in submarine sediments of some of these external (i.e., climatic or tectonic) forcing affecting aerial catchments depend on a myriad of processes which still remain difficult to extract from the deep sea record. To this end, one would need to evaluate not only how the eroded source responds to specific forcing but also how long and where are temporarily stored detrital sediments, and when are they re-injected into the system and eventually reach their sink.

Concerning the sediment source, mountainous catchments may not be very sensitive to high-frequency forcing, and the response time of these catchments may already affect the signal recorded in locally-produced sediments (e.g. Armitage et al., 2013; Godard and Tucker, 2021; Goren, 2016; Jerolmack and Paola, 2010). Second, transient sediment storage in piedmonts, alluvial plains, lakes or near the coast may induce a large time lag between the external signal and its record in the sedimentary sink (e.g. Blöthe and Korup, 2013; Clift and Giosan, 2014; Malatesta et al., 2018; Phillips and Slattery, 2006; Romans et al., 2016). Depending on considered timescales, the erosive signal itself can be completely buffered by this process (see a complete review in Romans et al. (2016)). Finally, submarine sediments can be reworked by gravitational processes, especially during sea-level falls (Phillips and Slattery, 2006). As a consequence, a significant part of the signal recorded in shallow-water sediments can be lost, whereas deep marine sediments may record simultaneously a signal coming from newly eroded source rocks and another one coming from the destabilization of previously deposited sediments. In addition, relative sea level variations may affect the connectivity between aerial rivers and submarine canyons, therefore limiting from time to time the efficiency of sediment transport in the offshore domain (Fryirs et al., 2007).

Detrital terrestrial cosmogenic nuclides (TCN, mostly ^{10}Be) concentrations from continental river sands or submarine sediments have been extensively used to determine the average long-term denudation rates of aerial catchments, provided enough quartz-bearing rocks outcrop at the surface to give a representative sampling of the whole catchment denudation (Bierman and Steig, 1996; von Blanckenburg, 2005; Lupker et al., 2012; Mandal et al., 2015; Siame et al., 2011; Vanacker et al., 2007). Denudation rate estimates from ^{10}Be concentration in quartz-rich sediments are often based on the assumption that the rate of TCN production by interaction of source rocks with cosmic radiations balances out the loss of these elements by surface denudation (Lal, 1991). Denudation rates can vary in time and space, which questions this steady-state assumption and may lead to under- or over-estimates of the true denudation rates (Bierman and Steig, 1996). The abundance of the target mineral (i.e., quartz in the case of ^{10}Be) in surface rocks may also vary, and has to be taken into account in order to correctly estimate the total production rate of a given catchment (Bierman and Steig, 1996; Carretier et al., 2015).

Moreover, sediments can be seen as an amalgamation of individual grains of different sizes and with different histories: allu-

vial terraces contain various clasts which TCN concentration is linked to the erosion rate of their catchment (inheritance) and to posterior TCN production (Repka et al., 1997). The distribution of TCN concentration in individual grains depend on the geomorphic processes acting at the source, and on the post-erosion TCN production (Codilean et al., 2010). Numerical models of individual grains journey have shown that some grains may have very long residence times in the piedmont (i.e., of the order of 100 ka) and may therefore be exported to their final depositional area long after they have been produced by bedrock erosion (Carretier et al., 2020). Landslides also may significantly affect denudation rate estimates from TCN if the catchment area is small (Yanites et al., 2009). Hence, understanding how detrital ^{10}Be concentrations recorded in submarine sedimentological archives reflect denudation rates at the time of their deposition requires to quantify: i) how, how fast and where ^{10}Be is produced; ii) how ^{10}Be concentration in produced sediments is representative of average catchment denudation rates at any given spatiotemporal scale (Zerathe et al., 2022) and iii) how long it has taken for sediments, once they are produced, to reach the sedimentary sink where they have potentially been sampled.

In this paper, we adapt the surface process model Badlands (Salles, 2016) to simulate erosion, deposition and detrital ^{10}Be transfer from a source-to-sink sediment system (the Var River catchment, Southern French Alps, and its marine depositional system in the Mediterranean sea) over the last 100 ka. We first compare real denudation rates with the ones that would be extracted from the ^{10}Be concentration of continental sediments (equivalent to river sands) or from off-shore deposited sediments at each time step, in order to assess at which timescales the steady-state assumption is valid, and if ^{10}Be record in detrital sediments provides an accurate estimate of continental denudation rates. Then, we examine which conditions (precipitation rate, flexure, ice cover) permit to satisfy published river incision rates (Cardinal et al., 2022; Petit et al., 2019; Rolland et al., 2017, 2020; Saillard et al., 2014) and ^{10}Be concentration in marine sediments (named hereafter $^{10}\text{Be}_{\text{MS}}$) in this particular, small-scale source-to-sink system (Mariotti et al., 2021).

2 Geomorphological and Geological setting

The Var catchment in Southern French Alps is ideally suited to constrain source-to-sink processes: it is a relatively small catchment ($\sim 2800 \text{ km}^2$), which encompasses some of the high altitude ($\sim 3000 \text{ m}$) summits of the Alpine Mercantour crystalline massif (Figure 1). The Var River has three main large tributaries: the Tinée and Vésubie Rivers, which headwaters are in the crystalline massif and the Esteron River, which flows only across the overlying meso-cenozoic sedimentary sequence. The hydric regime of the Var River, dominated by flash floods, is responsible for frequent hyperpycnal flows in the submarine domain (Mulder et al., 1998). The continental floodplain and shelf at the mouth of the Var River are underdeveloped and most detrital sediments are deposited offshore at the foot of the Ligurian margin (Mediterranean Sea), at depths below -2000 m . The average annual discharge at the mouth of the Var river is $\sim 50 \text{ m}^3 \cdot \text{s}^{-1}$, but it can reach more than $500 \text{ m}^3 \cdot \text{s}^{-1}$ during floods (Mulder et al., 1998). According to Mulder et al. (1998) and Syvitski et al. (2000), the suspended sediment load C_s can be obtained from the following expression:

$$C_s = aQ_w^b \quad (1)$$

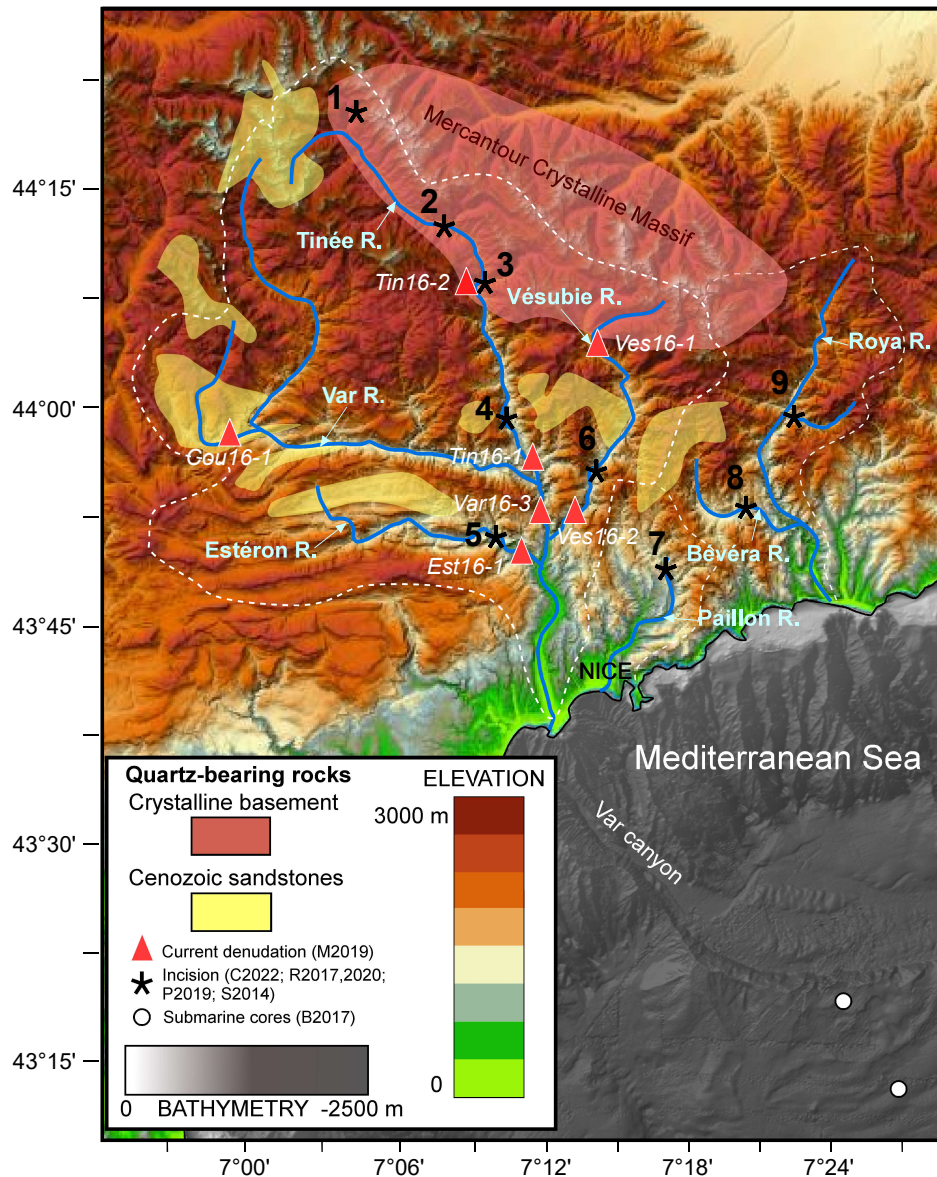


Figure 1. Topographic/bathymetric map and schematic outline of main quartz-bearing rock outcrops of the study area (transparent red and yellow patches). White dashed lines indicate the contours of the Var, Paillon and Roya Rivers catchments. Stars, open dots and triangles indicate the location of data constraints provided by surface exposure dating of river polished surfaces, after Saillard et al., 2014 (S2014), Rolland et al., 2017, 2020 (R2017,2020), Petit et al., 2019 (P2019), Cardinal et al., 2022 (C2022), geochemical analyses of submarine sediments after Bonneau et al., 2017 (B2017), and detrital ^{10}Be in river sands after Mariotti et al., 2019 (M2019), respectively. For river polished surfaces, the numbers refer to the following sites: 1 = Salso Moreno; 2 = Isola; 3 = Saint Sauveur; 4 = Lower Tinée; 5 = Estéron; 6 = Vésubie; 7 = Paillon; 8 = Bévéra; 9 = Roya. Italic letters refer to sample names in Mariotti et al. (2019).

where parameters a and b relate the sediment concentration C_s [$M.L^{-3}$] to mean discharge Q_w [$L^3.T^{-1}$] at the river mouth, and have been estimated to $\sim 7.7 \times 10^{-4}$ and ~ 1.65 for the Var River, respectively, from direct measurements of suspended sediment concentration and water discharge (Mulder et al., 1998). Modern average denudation rates estimates of the Var River catchment from ^{10}Be measurements in fluvial sediments range between 0.1 and 0.8 mm.yr^{-1} (Mariotti et al., 2019). Two other coastal rivers flow East of the Var catchment: the Paillon and Roya Rivers, with much smaller drainage areas (258 and 601 km^2 , respectively).

A previously published paper presented detailed sedimentological and geochemical analyses of sediment cores in the sedimentary ridge located at the outlet of the Var submarine canyon (Bonneau et al., 2016). These analyses revealed a larger frequency of turbidite flows and slightly larger Epsilon-Nd (ϵ_{Nd}) values during the Last Glacial Maximum (LGM), which is interpreted as reflecting more intense erosion, especially in the crystalline massif, and larger sediment production during glacial periods. In these cores, $^{10}\text{Be}_{\text{MS}}$ varies between 2×10^4 and 7×10^4 at.g^{-1} (atoms per gram of quartz), which corresponds to average denudation rates of 0.2 to 0.5 mm.yr^{-1} between 70 and 4 ka (Mariotti et al., 2021). On land, Cosmic Ray Exposure (CRE) ages of polished river cliffs have revealed fast incision rates of ~ 0.5 to 2 mm.yr^{-1} during the late Pleistocene in most sites of the Var catchment and in the Bévéra River (Cardinal et al., 2022; Petit et al., 2019; Rolland et al., 2017; Saillard et al., 2014). River gorges located at high altitudes in the Mercantour Massif (Sites 1 and 2 on Figure 1, red and brown dots on Figure 2) show very fast incision (up to 4 mm.yr^{-1}) starting after the Younger Dryas (YD), which can be ascribed to a transient response of formerly glaciated valleys. Most of lower altitude river gorges (Sites 3, 4, 5, 6, 8 on Figure 1, orange, yellow and green dots on Figure 2) start to be incised around 20 ka (i.e., close to the LGM). Two other sites (7 and 9 on Figure 1, cyan and blue dots on Figure 2) show much lower incision rates (< 0.5 mm.yr^{-1}) extending from 0 to 80 ka.

A possible interpretation of these data is that rivers which headwaters are in formerly glaciated areas (Tinée, Vésubie) incised faster during and after the LGM not only because of increasing precipitations but also because of the massive release of glacier meltwaters and stored sediments occurring at that time (e.g. Saillard et al., 2014; Rolland et al., 2020). More recently, Cardinal et al. (2022) have pointed out a complex response of river systems of the SW French Alps to deglaciations, depending on their connection with glaciated areas and on the presence of lithological knickpoints.

To summarize, river incision data suggest: 1) transient, post-YD and very fast incision in high altitude areas; 2) steady, fast incision rates at ~ 1 mm.yr^{-1} since the last 15-20 ka in almost all other points; 3) lower incision rates of ~ 0.2 to 0.5 mm.yr^{-1} in the Paillon and Roya Rivers, east of the Var catchment. Whatever the catchment, it appears that data points in the last ~ 20 ka range along slopes that define larger incision rates (sometimes by 1 order of magnitude) than average catchment denudation rates estimated from detrital ^{10}Be in river sands or marine sediments (Mariotti et al., 2019, 2021). This is not necessarily contradictory, as incision is a local phenomenon compared to the average catchment surface denudation. In particular, gorges where fast incision occurs can typically induce a transient decoupling from the catchment baselevel for the surrounding hill-slopes. However, there is a fundamental difference in the interpretation of river incision rates and $^{10}\text{Be}_{\text{MS}}$ from deep marine sediments: while gorges bedrock surface exposure ages in the last 20 ka define high incision rates, suggesting that the post-LGM period was characterized by enhanced incision and gorges entrenchment, the geochemical signature of marine sediments

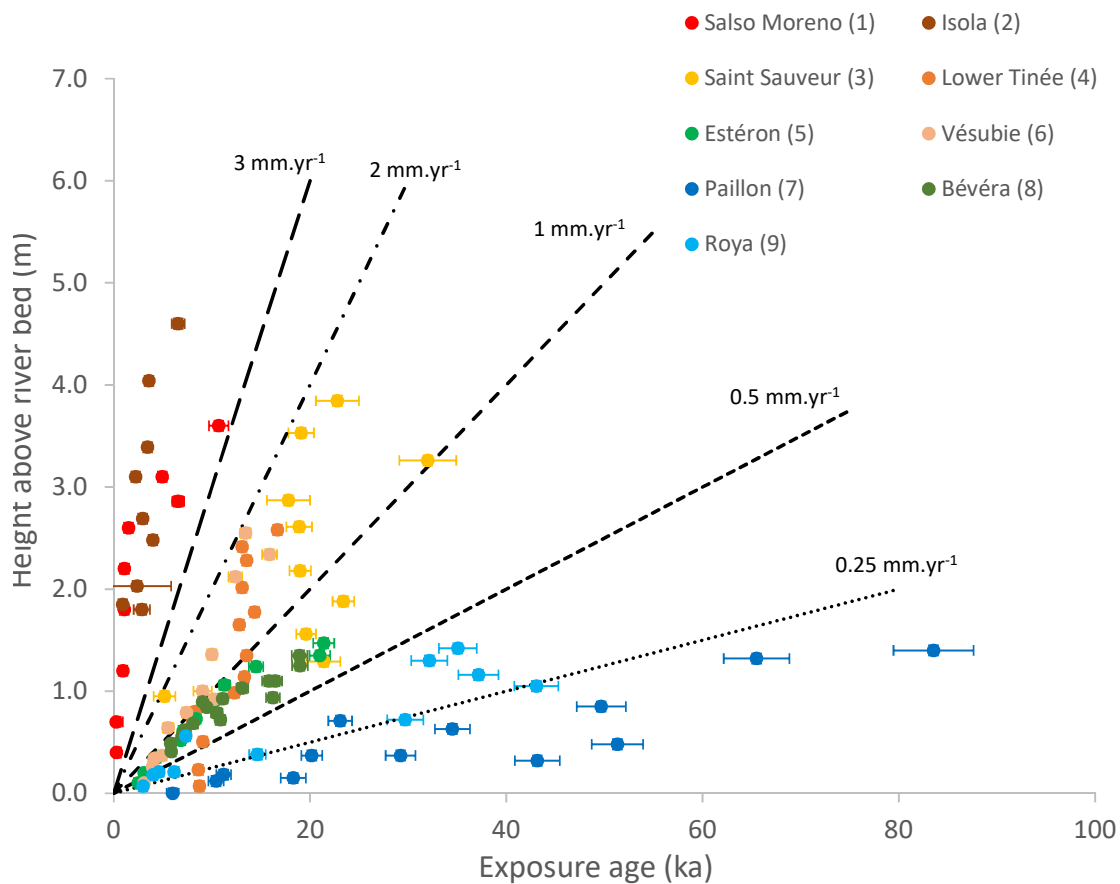


Figure 2. Altitude above the river bed vs. Cosmic Ray Exposure (CRE) ages and corresponding error bars in samples of river-polished surfaces of the Var, Roya and Paillon catchments (Cardinal et al., 2022; Rolland et al., 2020, 2017; Petit et al., 2019; Saillard et al., 2014). See location of the sites on Figure 1. Dashed lines indicate constant incision rate curves, for comparison.

is interpreted (Bonneau et al., 2016; Mariotti et al., 2021) as reflecting more intense erosion during the glacial episodes than during deglaciations.

3 Methods

125 3.1 Landscape evolution model

We use the Landscape Evolution Model (LEM) Badlands (Salles, 2016) to simulate erosion and deposition on an irregular TIN topographic grid under various tectonic (uplift) and climatic (precipitation, hillslope processes) time and space parameters. River incision is simulated using the Stream Power Law (Whipple and Tucker, 1999):

$$\varepsilon = K(\bar{P}.A)^m S^n \quad (2)$$

130 where ε is the erosion rate [$L.T^{-1}$], K is a dimensional coefficient that describes the erosional efficiency [$L^{1-2m}.T^{-1}$], A is the drainage area [L^2] and \bar{P} is the spatial and temporal variation in precipitation rate P relative to a mean precipitation rate P_0 (1 m.yr⁻¹), the product being used as a proxy for the discharge, S is the channel slope, m and n are positive exponents. A m value close to 0.5 was previously estimated in the Var and Vésubie catchments (Saillard et al., 2014; Petit et al., 2017), so we chose to set in all models m and n to classically used values of 0.5 and 1, respectively, and to tune the K value in order to fit
135 measured incision rates. Hillslope processes on land and short-distance sediment transport at sea can be simulated by a linear diffusion law:

$$\frac{dh}{dt} = K_D \nabla^2 h \quad (3)$$

where dh/dt is the altitude change due to diffusive processes [$L.T^{-1}$], h is the altitude [L] and K_D is the hillslope diffusion coefficient [$L^2.T^{-1}$], which can vary between the continental and marine domains. We fix the diffusion coefficient to low
140 values (0 to 0.025 m².yr⁻¹) both on land and at sea in order to insure that any observed smoothing effect on the ¹⁰Be record in deposited sediments is not due to diffusive processes (Table 2). For the same reason, we do not consider non-linear diffusion components. For river systems, we use the detachment-limited law (Eq. 2) but we impose sediment deposition either when the channel slope falls below a given threshold (alluvial plain deposition, see Table 3) or when the rivers reach their baselevel. A low critical slope of 0.5% is applied, except for two models where a very low threshold of 0.01 % is used in order to
145 drastically limit alluvial plain deposition. In addition, we take into account submarine sediment transport in order to simulate the occurrence of hyperpycnal flows. Following an approach similar to Petit et al. (2015) and Thran et al. (2020), we assume that hyperpycnal flows occur when the sediment load at the river mouth is larger than a given threshold. If the flow density exceeds this threshold, instead of being deposited near the baselevel, sediments continue their route along the submarine slope. In addition, we assume that the flow does not incorporate water along its path. The flow density at the river mouth ρ_f [$M.L^{-3}$]
150 can be computed: i) either with a mass estimate from water and sediment discharge (Q_w and Q_s , respectively [$L^3.T^{-1}$]) and densities (ρ_w and ρ_s , respectively):

$$\rho_f = \frac{\rho_w \cdot Q_w + \rho_s \cdot Q_s}{Q_w + Q_s} \quad (4)$$

or using the rating parameters a and b (Syvitski et al., 2000), which can be determined for each river system from discharge and sediment load measurements. While Eq. 4 considers the total mass of sediment transported by the river (i.e., bedload and suspended load), the rating parameters allow an empirical estimation of the suspended load, the one that effectively contributes to the increase in flow density. We consider that submarine flow can trigger bedrock erosion as for aerial channels, but the parameters of the stream power law are adjusted in order to account for: 1) constant drainage area along channel length in the submarine domain and 2) lower shear stress on the submarine channel bed compared to aerial rivers, which is simplified assuming an effective slope S_{eff} such that:

$$S_{eff} = S \frac{\rho_s - \rho_w}{\rho_s} \quad (5)$$

Deposition occurs in the submarine domain either for gentle slopes (similar to alluvial plains on land) and beneath a certain depth (-2300 m in most models) corresponding to the depth of the abyssal plain. Flexural isostasy can be incorporated with a constant or space-variable effective elastic thickness (EET) used to compute the vertical motion resulting from the response of the lithosphere to loading (by ice, sedimentation or sea level rise) or unloading (deglaciation, erosion or sea level drop). Flexural isostatic response of the lithosphere is computed using the flexure equation:

$$D \nabla^4 w(x, y) + \Delta \rho g w(x, y) = L(x, y) \quad (6)$$

Where w is the vertical deflection, $\Delta \rho$ is the density contrast between the mantle and the filling material, L is the load (N) and D is the flexural rigidity of the lithosphere (N.m):

$$D = E \cdot EET^3 / 12(1 - \nu^2) \quad (7)$$

With E the Young's modulus and ν the Poisson's ratio, equal to 10^{11} Pa and 0.25, respectively. The flexure module in Badlands uses the gFlex package (Wickert, 2016). Apart from flexural response to erosion/sedimentation and ice and sea water loading and unloading during the model run, no vertical motions are applied to the topography.

3.2 Ice cover and sea level changes

As the Mercantour massif was periodically covered by glaciers during the Quaternary, we simulate the ice thickness and extent at every time step assuming that the LGM corresponds to the maximum ice extent map (Brisset et al., 2015). We consider that ice thickness varies with Mediterranean sea surface temperatures (SST), which ranged between $\sim 5^\circ\text{C}$ (LGM) and $\sim 15^\circ\text{C}$ during the considered time period (Hayes et al., 2015; Rodrigo-Gamiz et al., 2013). Glacial periods with full ice extent are imposed for SST lower than 6.5°C and complete deglaciation for SST above 11°C . Between these thresholds, the ice thickness is assumed to vary linearly with the SST. In order to avoid fast variations of the ice cover, the SST curve is smoothed using a 5 kyr sampling interval which is then resampled at 1 kyr step using cubic interpolation (Figure 3). When ice thaws, an equivalent amount of water (assuming a ratio between the ice and water heights of 0.93) is released and participates to runoff. Sea level variations can be imposed according to the Mediterranean eustatic sea level curve published in Waelbroeck et al. (2002). Badlands does not simulate glacial erosion; however, we must consider a non-null erosion rate beneath glaciated areas

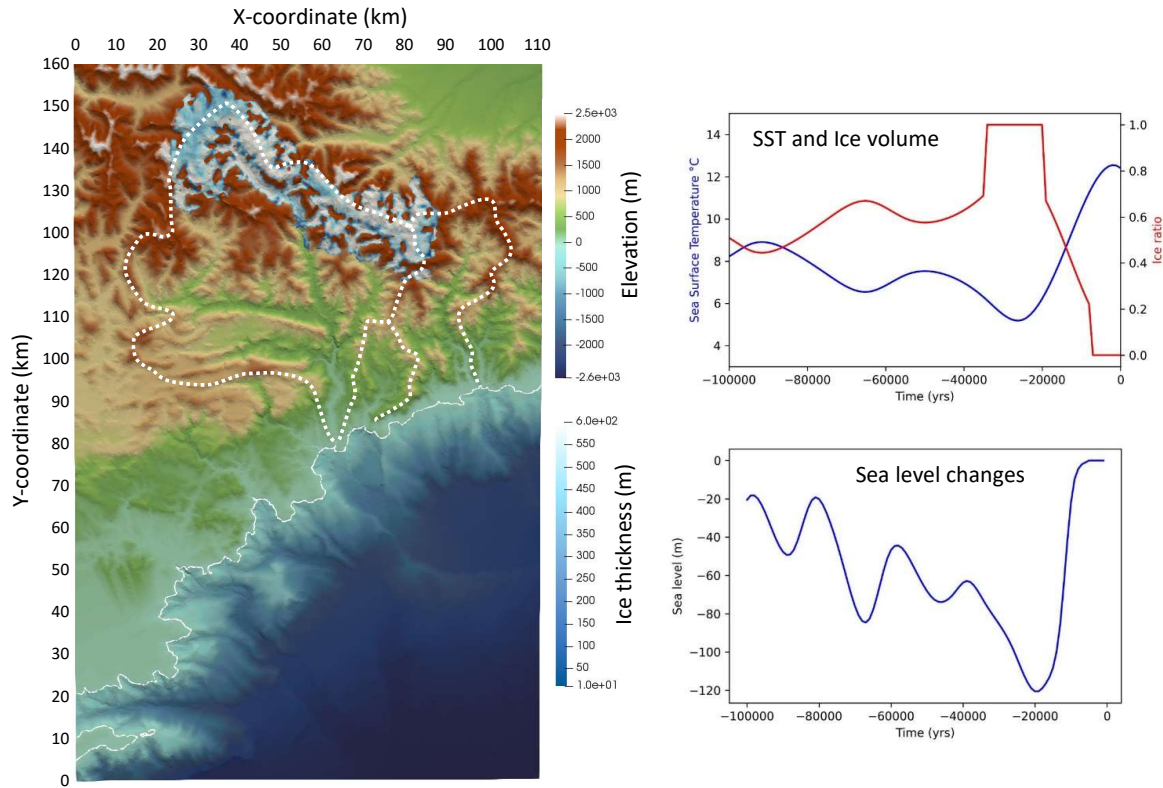


Figure 3. Left : Topography, bathymetry and maximum ice thickness (after Brisset et al., 2015), and contour of the main catchments (dashed line); Top right: smoothed variations of the sea surface temperature (SST, after Hayes et al., 2005 and Rodrigo-Gamiz et al., 2013) in blue and ice thickness ratio (1 is for full ice, 0 for no ice) in red; bottom right: sea level variations (after Waelbroeck et al., 2002).

in order to avoid over-estimation of the ^{10}Be concentration in sediments produced by basement erosion after glaciers retreat.

185 For this purpose, we simulate the in-situ erosion and sediment production due to glacial processes by increasing the local hillslope diffusion coefficient proportionally to the ice thickness, which will locally enhance denudation beneath glaciated areas, while river discharge is set to zero. This simplified representation is based on the assumption that glacial sediments fluxes are proportional to the topographic slope (hence to ice velocity) and that glacial erosion is related to the shear stress exerted by the glacier on the bedrock (Boulton, 1996). Besides erosion, the effect of ice coverage is twofold: it blocks cosmic radiations so ^{10}Be production is null beneath in areas covered by glaciers, and it creates a positive vertical load and downward flexure of the lithosphere.

190

3.3 ¹⁰Be production and transport

¹⁰Be production rates by neutron spallation and muon capture are the same as in Mariotti et al. (2019) and computed according to Braucher et al. (2011); Martin et al. (2017) for a latitude of 40° (Table 1) using the scaling parameters by Stone (2000). Earth magnetic field variations are not considered in this study. The topographic shielding is computed from the TIN topographic grid. A shielding correction can be applied to account for the topographic smoothing due to the DEM resolution, which tends to underestimate the actual shielding (Norton and Vanacker, 2009).

A map of quartz-bearing rocks is defined according to the geological map of Nice and its hinterland (Rouire et al., 1980); most quartz-bearing rocks correspond either to granitic and metamorphic Palaeozoic basement rocks in the Mercantour massif or to Cenozoic sandstones in the sedimentary cover (Figure 1). The average quartz concentration in source rocks is fixed at 50%. The initial ¹⁰Be concentration in quartz-bearing rocks is computed assuming a steady-state average denudation rate for the whole grid. ¹⁰Be concentration $N(z,t)$ varies with time and depth, and we simply compute it at the surface ($z=0$) of eroded domains (Lal, 1991):

$$\frac{dN(0,t)}{dt} = P(0,t) - \left(\lambda + \frac{\rho \cdot \varepsilon(t)}{\Lambda} \right) N(0,t) \quad (8)$$

where N is the ¹⁰Be concentration (at.g^{-1}), P is the production rate ($\text{at.g}^{-1}.\text{yr}^{-1}$), λ is the ¹⁰Be radioactive decay constant (yr^{-1}), ρ the rock density (g.cm^{-3}), Λ is the attenuation length (g.cm^{-2}), and ε the erosion rate (cm.yr^{-1}). At each time step, the production rate is computed taking into account the quartz abundance of the source rock and the potential shielding of cosmic rays by the surrounding topography, and/or by the ice or sea cover.

¹⁰Be production results primarily from neutron spallation, and fast and slow muon capture with different production rates and attenuation lengths (Braucher et al., 2011) (Table 1). Assuming that erosion and production rates are constant during a given time step of the model, we can compute explicitly the ¹⁰Be concentration in each eroded node of the source rocks at each time step, without any a priori steady-state assumption (Knudsen et al., 2019):

$$N(0,t) = N(0,t - \Delta t) \cdot \exp \left[- \left(\lambda + \frac{\rho \cdot \varepsilon(t)}{\Lambda} \right) \Delta t \right] + \frac{P(0,t)}{\lambda + \frac{\rho \varepsilon(t)}{\Lambda}} \cdot \left(1 - \exp \left[- \left(\lambda + \frac{\rho \varepsilon(t)}{\Lambda} \right) \Delta t \right] \right) \quad (9)$$

This Eulerian formulation, where the erosion rate ε is equal to the vertical velocity at which the rock material is vertically advected up to the surface is chosen because it does not necessitate to compute vertical concentration profiles for each grid point.

For the initial ¹⁰Be concentration $N(0,0)$ we assume steady-state between ¹⁰Be production and erosion by imposing a mean long-term erosion rate ε_0 :

$$N(0,0) = \frac{P(0,0)}{\frac{\rho \cdot \varepsilon_0}{\Lambda} + \lambda} \quad (10)$$

At each time step, the total sediment, quartz and ¹⁰Be fluxes are computed on each grid node. In the case of deposited sediments, we then compute the mean detrital ¹⁰Be concentration and quartz content of sediments, knowing the volume contribution, quartz proportion and ¹⁰Be concentration of each eroded source to the total amount of deposited sediments, assuming a perfect mixing

between all sources. We use as initial conditions a smoothed topographic and bathymetric DEM with a spatial resolution of 500 m x 500 m.

225 In a first test, a simulation is run with a constant precipitation rate of 0.5 m.yr^{-1} over 5000 years with a timestep of 100 years in order to calibrate SPL parameters, mainly the erodibility coefficient K against the results of Mariotti et al. (2019). From this model (M1), we compute the ^{10}Be production rate in the Mercantour massif, the mean ^{10}Be concentration of continental river sediments corresponding to the catchments sampled by Mariotti et al. (2019) and the related mean catchment denudation rate deduced from these concentrations, with an initial steady-state ^{10}Be concentration computed using a mean denudation rate of
 230 0.2 mm.yr^{-1} , in agreement with Mariotti et al. (2019) (Figure 4 and Table 2). Data from the Coulomp River, a small tributary of the Var River, could not be satisfyingly reproduced (Table 2, Cou-16.1): the predicted low ^{10}Be concentration resulted in a denudation rate **more than twice as high as in Mariotti et al. (2019)**. Similarly, one point in the Vesubie River (Ves-16.1), which has a large ^{10}Be production rate, shows a modelled ^{10}Be **concentration slightly larger than measured by Mariotti et al. (2019)**. As a consequence, the erosion rate for this point is underestimated (Figure 4). While not perfect, simulated estimates
 235 **of ^{10}Be production and erosion rates provide a good fit with observations** and allow us to constrain the value of K . Several improvements might reduce the observed discrepancies, first by using a higher DEM resolution and second by accounting for underground (karstic) water circulation known to take place in the region like for the Coulomp River (Audra et al., 2009), which should modify river discharge and related incision rates.

Table 1. Sea level high latitude parameters for ^{10}Be production (after Braucher et al. (2011))

Neutron spallation rate $at.g^{-1}.a^{-1}$	Slow muon capture rate $at.g^{-1}.a^{-1}$	Fast muon capture rate $at.g^{-1}.a^{-1}$	Neutron attenuation length $g.cm^{-2}$	Slow muon attenuation length $g.cm^{-2}$	Fast muon attenuation length $g.cm^{-2}$	Radioactive decay constant a^{-1}	Density $g.cm^{-2}$
4.11 ± 0.19	0.011 ± 0.001	0.039 ± 0.004	160	1500	4320	4.9867×10^{-7}	2.5

4 Results

240 4.1 Record of time variable erosion rates in river sands and at sea

We then test the response of a topographic grid representing the Var aerial and submarine systems to climatic (precipitation) variations. The model runs for 100 kyr with an adaptive time step of max. 1000 years. We keep a constant rock erodibility of $5 \times 10^{-6} \text{ yr}^{-1}$ and a hillslope diffusion coefficient of $2.5 \times 10^{-2} \text{ m}^2.\text{yr}^{-1}$. The river sediment load is computed from water discharge using rating parameters (Syvitski et al., 2000) for the Var River a and b equal to 1×10^{-3} and 1.6, respectively, and a
 245 low threshold flow density (equal to water density), which insures that all river sediments are exported to the deep submarine basin and that no large river delta is formed near the coastline.

In a first series of tests, we want to investigate how well the ^{10}Be concentrations in continental (i.e., in river sand) and submarine

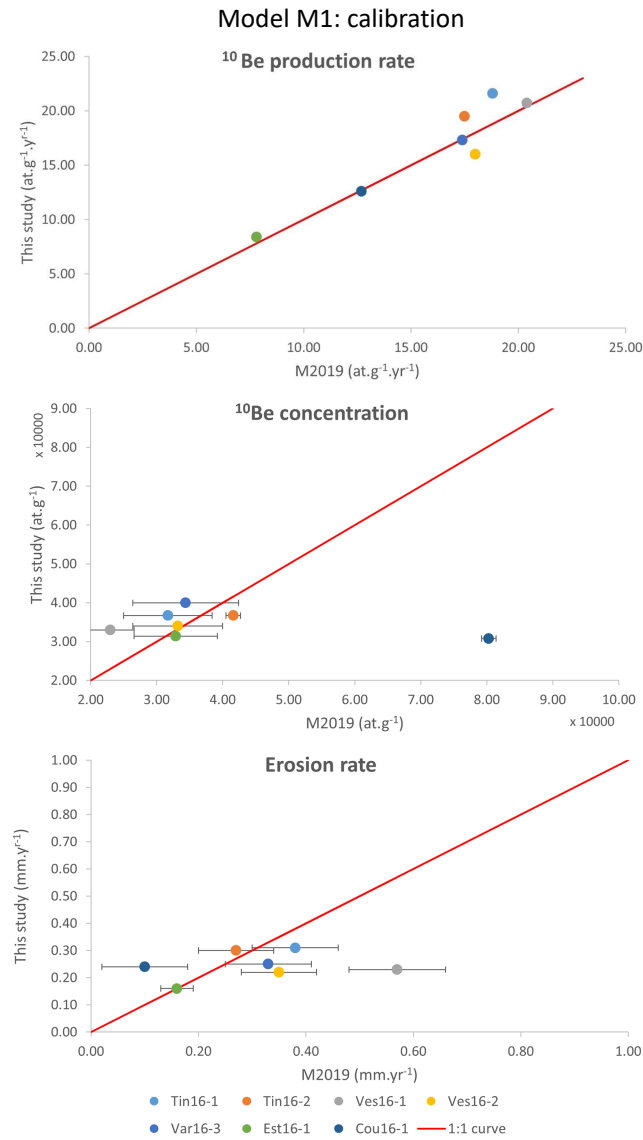


Figure 4. Comparison between the results of Mariotti et al. (2019) (x-axis) and the short-term model (this study, y-axis) for several rivers of the Var catchment, for ^{10}Be production rates (top), ^{10}Be concentration in river sediments (middle) and steady-state erosion rates (bottom). Red line indicates the 1:1 slope. See Table 2 for values.

Table 2. Calibration of ^{10}Be production and erosion rates after the results of Mariotti et al. (2019) for the present-day rates

Sample site	Production rate		^{10}Be concentration		Erosion rate	
	$\text{at.g}^{-1}.\text{yr}^{-1}$		at.g^{-1}		mm.yr^{-1}	
	M2019	This study	M2019	This study	M2019	This study
Tin16-1	18.8	21.6	$(3.17\pm 0.67)\times 10^4$	3.67×10^4	0.38 ± 0.08	0.31
Tin16-2	17.5	19.5	$(4.16\pm 0.11)\times 10^4$	3.67×10^4	0.27 ± 0.07	0.30
Ves16-1	20.4	20.7	$(2.3\pm 0.36)\times 10^4$	3.30×10^4	0.57 ± 0.09	0.23
Ves16-2	18.0	16.0	$(3.32\pm 0.68)\times 10^4$	3.40×10^4	0.35 ± 0.07	0.22
Var16-3	17.4	17.3	$(3.44\pm 0.80)\times 10^4$	4.00×10^4	0.33 ± 0.08	0.25
Est16-1	7.8	8.4	$(3.29\pm 0.63)\times 10^4$	3.14×10^4	0.16 ± 0.03	0.16
Cou16-1	12.7	12.6	$(8.03\pm 0.11)\times 10^4$	3.08×10^4	0.10 ± 0.08	0.24

Table 3. Model parameters

Figure	Model	Precipitation m.yr^{-1}	Erodibility yr^{-1}	Diffusion coefficient $\text{m}^2.\text{yr}^{-1}$		Critical slope	Deposition depth (m)	Sea level changes	Ice cover	Flexure
				aerial	marine					
4	M1	0.5	4.5×10^{-6}	0	2.5×10^{-2}	0.005	-2300	No	No	No
6A	M2	0.25/1	5.0×10^{-6}	0	2.5×10^{-2}	0.005	-2300	No	No	No
6B	M3	0.25/1	5.0×10^{-6}	0	2.5×10^{-2}	0.005	-2300	Yes	No	No
6C	M4	0.25/1	5.0×10^{-6}	0	2.5×10^{-2}	0.005	-2300	Yes	Yes	No
6D	M5	0.25/1	5.0×10^{-6}	0	2.5×10^{-2}	0.005	-2300	Yes	Yes	Yes
6E	M6	0.25/1	5.0×10^{-6}	0	2.5×10^{-2}	0.0001	-200	No	No	No
6F	M7	0.25/1	5.0×10^{-6}	0	2.5×10^{-2}	0.0001	-800	No	No	No
7	M8	0.5	5.0×10^{-6}	0	2.5×10^{-2}	0.005	-2300	Yes	Yes	Yes
8-9A	M9	0.3/0.7	3.5×10^{-6}	1.0×10^{-3}	2.5×10^{-2}	0.005	-2300	Yes	Yes	Yes
9B	M10	0.3/0.7	3.5×10^{-6}	1.0×10^{-3}	2.5×10^{-2}	0.005	-2300	Yes	Yes	No
9C	M11	0.3/0.7	3.5×10^{-6}	1.0×10^{-3}	2.5×10^{-2}	0.005	-2300	Yes	No	Yes
9D	M12	0.3/0.7	3.5×10^{-6}	1.0×10^{-3}	2.5×10^{-2}	0.005	-2300	No	Yes	Yes
9E	M13	0.5	3.5×10^{-6}	1.0×10^{-3}	2.5×10^{-2}	0.005	-2300	Yes	Yes	Yes
9F	M14	0.3/0.7	3.5×10^{-6}	1.0×10^{-3}	2.5×10^{-2}	0.005	-2300	Yes	No	No
9G	M15	0.3/0.7	3.5×10^{-6}	1.0×10^{-3}	2.5×10^{-2}	0.005	-2300	No	Yes	No

(turbidite-like) deposits compare with the average catchment denudation rate directly output from the model. For this purpose, we select the total area of the Var catchment where ^{10}Be is produced and compute the average ^{10}Be concentration N_{ex} in

250 the volume of rock eroded from this source for each time step (hereafter called "in-situ" sediments, because they are not yet transported nor deposited), from the contribution of each catchment node i such as:

$$\overline{N_{ex}} = \frac{\sum_{i=1}^n N_i \varepsilon_i Q_i}{\sum_{i=1}^n \varepsilon_i Q_i} \quad (11)$$

where Q_i is the quartz abundance, N_i is the ^{10}Be concentration (at.g^{-1}) and ε_i the eroded mass of sediments (in g). Then we use Eq. 10 to compute the catchment denudation rate assuming a steady-state condition, and compare it with the average
255 "actual" denudation rate directly output from the model (i.e., the average volume of eroded sediments in the same area per time step). Finally, we extract the average $^{10}\text{Be}_{\text{MS}}$ value in 8×8 km square areas located at the mouth of the Var River for model M6, in the submarine canyon for model M7 and in the deep submarine basin for models M2 to M5. We then use the same equation to compute the average catchment denudation rate as recorded by deep sea sediments (as shown in Figure 5). Simulations are run with alternating low (0.25 m.yr^{-1}) and high (1 m.yr^{-1}) precipitation rate periods lasting 20 kyr each (Figure 6). The first
260 simulation (M2) is run with a constant sea level, no ice cover and no lithospheric flexure; then we successively implement a variable Mediterranean sea-level, ice cover in the Mercantour massif (M3 and M4, see Figure 3) and lithospheric flexure with a constant EET of 20 km (M5), which corresponds to a moderately rigid lithosphere where the crust and mantle elastic lids are decoupled (Burov and Diament, 1995). The last two models of this series (M6 and M7) have similar parameters as M2, except that i) we drastically decrease the slope threshold for alluvial plain deposition, which almost impedes sediment storage on-land
265 and ii) we force deposition in the submarine domain at shallower depths: either in the coastal delta (-200 m) for M6 or in the submarine canyon (-800 m) for M7.

The first model (M2, Figure 6A), where there are no sea level changes, no ice cover and no flexural isostatic response of the lithosphere shows that the two periods of more intense precipitations are well-detected in in-situ sediments, which ^{10}Be signature gives erosion rates consistent with the actual ones. Marine sediments also seem to record two periods of larger erosion
270 rates, but the first one (between 25 and 45 ka) is barely visible and the peak of the second one (80-90 ka) occurs 10 to 20 ka after the middle of the second high-precipitation period. The second model (M3, Figure 6B) where sea level variations are present displays approximately the same behaviour as M2 for in-situ sediments, with apparent erosion rates consistent with real ones. Erosion rates computed from marine sediments also show fluctuations consistent with two periods of more intense precipitations, but they appear much smoother and offset by 20 ka, compared to the actual ones. In the two following models
275 where ice cover is present (M4 and M5, Figures 6C and 6D), the effect of partial coverage of the Mercantour massif by ice during almost all the duration of the model is twofold: i) it reduces the effect of precipitation variations, since no run-off occurs beneath the ice cover and ii) it reduces the production and exportation of ^{10}Be -poor sediments, except during the last period (80-100ka) where the massif is free of ice. As a consequence, while in-situ sediments still record well the actual erosion rate, the ^{10}Be signal in the submarine domain strongly under-estimates it. Finally, models similar to M2 but with a lower critical
280 slope and where sediment deposition is forced either in the delta (M6) or in the submarine canyon (M7) show that marine sediments of the delta record well the onset of first precipitation pulse, with only a small time lag (5 ka). Then, the apparent erosion rate computed from marine sediments progressively decreases and the second period of intense precipitation is not recorded. In this model, ^{10}Be -poor sediments coming from the second precipitation pulse are not deposited in the sampled area

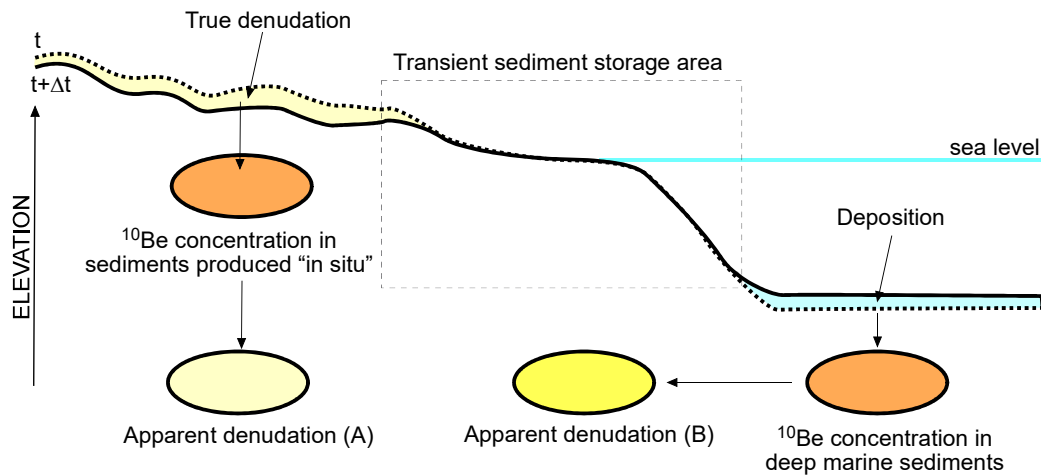


Figure 5. Schematic description of the approach used to compare the apparent denudation for a given time step computed from the mean ^{10}Be concentration of in-situ produced sediments (left part of the topographic profile, apparent denudation A) or from the mean ^{10}Be concentration of marine sediments ($^{10}\text{Be}_{\text{MS}}$, right part of the profile, apparent denudation B) with the true denudation.

but further south, due to delta progradation. Finally, if deposition is forced to occur in the middle of the submarine slope, the
 285 first precipitation peak is still detected but it appears smoother, of lower amplitude, and it occurs 20 ka later than on land (Figure 6F).

In simulations without ice cover (Figures 6A, 6B, 6E and 6F), denudation rates estimated from in-situ sediments do record the succession of periodic pulses but generally overestimate the actual denudation rate by a few percent. This overestimation reflects a more intense erosion in low-altitude river thalwegs than on the hillslopes and high-altitude interfluves, which slightly
 290 promotes the export of ^{10}Be -poor sediments with respect to ^{10}Be -rich ones, hence increasing the apparent denudation rate.

For all simulations, both in-situ and actual denudation rate evolutions depict more complex patterns than the imposed climatic (precipitation) forcing. Short-period, low-amplitude variations are visible, which are related to local and internal adjustments of the modelled topography and not to the external forcing, although sea level variations seem to slightly modify their amplitude (Figures 6A and 6B). There is no clear time lag between the onset of higher precipitation periods and their record in in-situ
 295 sediments, but the apparent denudation rate from in-situ river sediments displays a curved shape at the transition between low and high precipitation rate periods (well visible for instance on figure 6A between 60 and 80 ka), which corresponds to well-known analytical solutions for periodic changes in erosion rates (Bierman and Steig, 1996) and is consistent with the detachment-limited hypothesis. This reflects the time needed for ^{10}Be concentration to reach a steady-state relative to the massif denudation rate (~ 5 ka); this effect is also visible at the transition from high to low precipitation rates (Figures 6E and
 300 6F).

This series of tests seem to indicate that: i) the in-situ produced alluvial sediments record well the variations in the rate of denudation, although they may slightly overestimate them; ii) ^{10}Be of submarine sediments $^{10}\text{Be}_{\text{MS}}$ in the deepest part of the basin does not allow to retrieve sharp climate variations especially if glaciers cover the area where ^{10}Be is produced for a long period of time, but correctly estimate the average long-term erosion rate, with only smooth variations; iii) finally, there can
305 be a significant time lag between the middle of the high precipitation periods and the peak in denudation rates recorded in submarine sediments.

In order to refine our understanding of the smoothing and time lag effects, we aimed at tracing artificially-enriched ^{10}Be -rich sediments in the mountain range down to the submarine basin. To do so, we imposed a constant and artificial, large ^{10}Be concentration in high-altitude **reliefs** (above 1800 m) over a 5 kyr period from 30 to 35 ka. Then, we compare the ^{10}Be
310 signature of deep-sea sediments between two identical models, one ran with the ^{10}Be enrichment and one without (model M8, Figure 7). We do not show all the tests here for the sake of simplicity, but rather illustrate a typical signature of this transient ^{10}Be enrichment, as visible in submarine sediments. This result is obtained accounting for a variable sea level, ice cover and lithospheric flexure, and a constant precipitation rate of 0.5 m.yr^{-1} (Table 3). If we consider the earliest arrival of ^{10}Be -rich sediments in the submarine basin, the time lag from source to sink appears to be relatively small (1-3 kyr) since ^{10}Be -rich
315 sediments arrive in the basin shortly after they begin to be produced in the massif (Figure 7); however, the time lag between the middle of the ^{10}Be enrichment period on-land and the largest ^{10}Be peak recorded in marine sediments is rather large (~10 kyr). Moreover, this signal takes a long time to relax: sediments that are richer in ^{10}Be than the reference simulation still reach the basin ~25 kyr after the end of the enrichment period. These tests suggest that, although the initial time lag is not necessarily very important, the relaxation time i.e., the **time it takes for the ^{10}Be concentration to return to its normal value can be so large**
320 **that the submarine ^{10}Be signal could bear the superimposed effect of separate past events.** We want to stress here that this delay is different from the time needed to reach cosmogenic radionuclides steady state, as computed in Bierman and Steig (1996). Here, we do not force high ^{10}Be concentration in the Mercantour massif by reducing drastically the erosion rate - which would indeed take some time for the ^{10}Be signal to adapt and reach a new steady-state. Instead, we instantaneously apply a large, artificial ^{10}Be value in the mountain peaks, which should be immediately visible in deposited sediments if the time lag was
325 null.

4.2 Reference model for the Var catchment over the last 100 ka

Finally, we try to determine if it is possible to find model parameters for which the result matches both the previously determined river incision rates during the last 30-40 ka in the Nice hinterland (Figure 2) and measured $^{10}\text{Be}_{\text{MS}}$ for the same period (Mariotti et al., 2021). We chose not to consider the two river gorge sites that have been dated in the upper Tinée valley (Salso
330 Moreno and Isola, see Figure 1), because they likely correspond to very transient post-glacial sediment wash-out that is not possible to model (Rolland et al., 2020). This "Reference" model has been determined by a trial-and-error method, with initial and boundary conditions similar to the previous series of runs (Figures 8 and 9A, model m9). Sea level variations and ice cover are imposed, and simulations are run for 100 kyr with a time step of 1 kyr. We assume that for the last period of the model, which corresponds to the present-day situation, the precipitation rate should be compatible with current average values

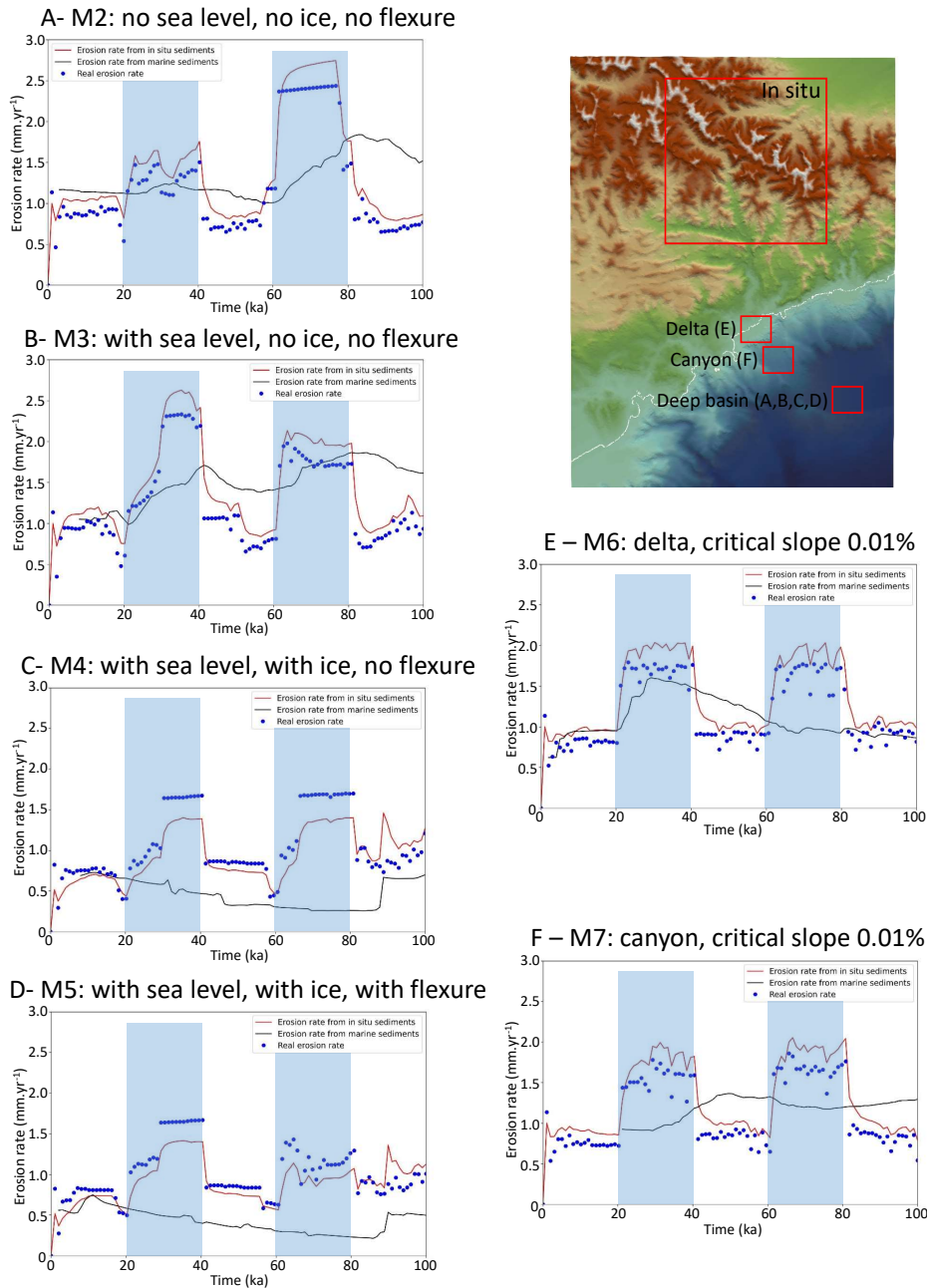


Figure 6. Test of the apparent denudation rates given by the ^{10}Be concentration of in-situ (red line) and deep marine ($^{10}\text{Be}_{\text{MS}}$, black line) sediments, versus the actual one extracted from the model (blue dots). Periods of large precipitation rates are indicated by the transparent blue rectangles. A: model with only variable precipitation rate; B: model with variable precipitation rate and sea level variations; C: model with variable precipitation rate, ice cover and sea level variations; D: model with variable precipitation rate, sea level variations, ice cover and flexure; E: model similar to A but with a lower critical slope for sediment deposition, and forced deposition below -200m; F: model similar to E but with forced deposition below -800m.

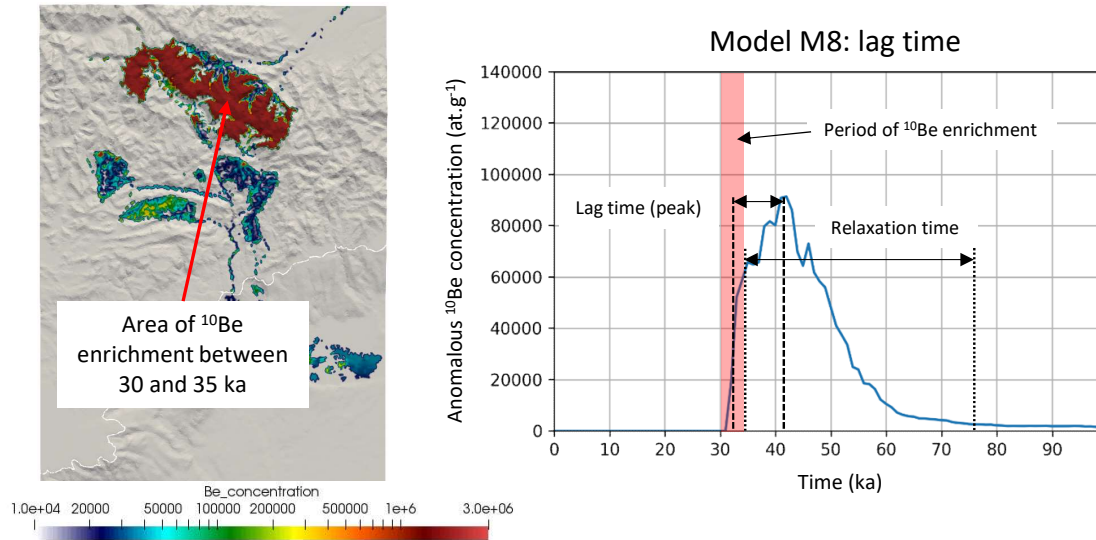


Figure 7. Difference in $^{10}\text{Be}_{\text{MS}}$ between two models with the same parameters (Table 3), one of them having an imposed ^{10}Be -rich (2×10^6 at.g $^{-1}$) rocks above 1800 m between 30 and 35 ka (red transparent rectangle). Left panel shows the location of the area of ^{10}Be enrichment in the Mercantour massif. The time lag (thick dashes) is defined as the interval between the middle of the ^{10}Be enrichment period in the massif and the age of the largest ^{10}Be peak in marine sediments. The relaxation time is defined as the interval between the end of the ^{10}Be enrichment period in the massif and the end of excess ^{10}Be recorded in marine sediments.

335 (i.e., 700-800mm.yr $^{-1}$, <https://meteofrance.com/climat/normales/france/provence-alpes-cote-d-azur/NICE>). Here again, flexural isostatic response is computed using a constant effective elastic thickness of 20 km. We also tested different EET values of 10 and 30 km as well as a space-variable EET, with larger values on land than at sea. Since variations in EET are difficult to constrain and cause only minor differences in the final result, we chose to impose this constant value of 20 km on the entire grid for all models. We first present a model which satisfyingly reproduces measured river incision rates and ^{10}Be measurements, then we discuss the implications of each parameter (flexure, sea level, ice cover) in the final result. This simulation involves a precipitation rate of 0.3 m.yr $^{-1}$ from 0 to 80 kyr increasing to 0.7 m.yr $^{-1}$ during the last 20 kyr, an initial denudation rate of 0.2 mm.yr $^{-1}$, a diffusion coefficient of 2.5×10^{-2} m 2 .yr $^{-1}$ in submarine and river sediments and of 0.1 m 2 .yr $^{-1}$ in bedrock areas and a constant erodibility coefficient of 3.5×10^{-6} yr $^{-1}$ (Figures 8 and 9A and Table 3). This model satisfyingly reproduces measured incision rates in river channels and yields a slight increase in $^{10}\text{Be}_{\text{MS}}$ in the Var deep sea fan after ~ 40 ka (Figure 345 9A). Given the large variability of $^{10}\text{Be}_{\text{MS}}$ values (as depicted by the standard error bars), the modelled $^{10}\text{Be}_{\text{MS}}$ variation is compatible with almost all measurements published in Mariotti et al. (2021). From the simulation outputs, we find that the increase in $^{10}\text{Be}_{\text{MS}}$ is not due to a change in erosion rate on land: indeed, river incision rates tend to increase after 20 ka due to the release of glacier meltwaters and to increased precipitation rates, while the $^{10}\text{Be}_{\text{MS}}$ also increases twofold. The observed

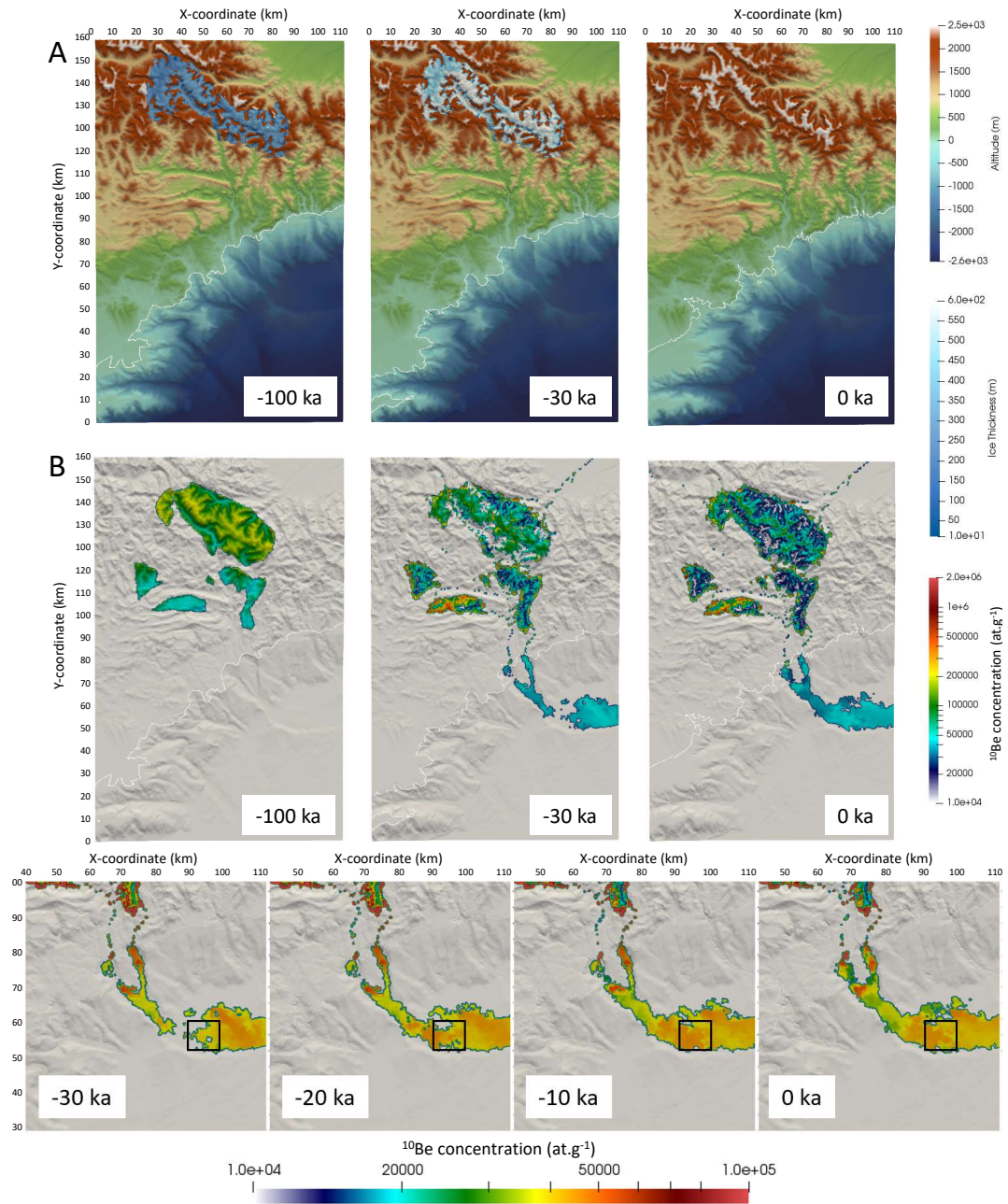


Figure 8. Stages of evolution of the reference model from 0 to 100 ka (model time, corresponding to -100 to 0 ka in reality). Upper panels (A) present the topography and ice thickness, middle panels (B) present the surface ^{10}Be concentration and lower panels (C) present a blow-up of the surface ^{10}Be concentration in submarine sediments in the last 30 ka, with an adjusted color map. Solid rectangle on the lower panels indicates the area where average $^{10}\text{Be}_{\text{MS}}$ has been computed (see results on Figure 9).

increase in $^{10}\text{Be}_{\text{MS}}$ around 30-40 ka is, in fact, due to the presence of patches of ^{10}Be -rich sediments deposited in the upper part of the basin in the early stages of the model, which slowly feed lower areas of the basin in ^{10}Be -rich sediments during the run (Figure 8B and 8C). The simulation fit with the measured $^{10}\text{Be}_{\text{MS}}$ may somehow be fortuitous, since the surface concentration in ^{10}Be varies a lot, both locally and vertically. This simulation thus shows that: 1) ^{10}Be concentration at the surface of the submarine basin at a given time can be highly variable; hence, the vertical variation of $^{10}\text{Be}_{\text{MS}}$ can also be variable from one place to another, and 2) it is quite possible to get both increased incision rates on-land and apparent decreased denudation rates in submarine cores, for the same external (climatic) forcing.

Starting from this reference simulation (Figure 9A), we then evaluate the individual effects of lithospheric flexure, ice cover and sea level changes. A similar simulation without lithospheric flexure predicts slightly lower incision rates for all rivers, with a more dramatic change for the Vésubie River where it drastically decreases (Figure 9B, model M10); meanwhile, both the absolute values of $^{10}\text{Be}_{\text{MS}}$ and their variations are still consistent with measurements. A simulation similar to the reference one but without ice cover (Figure 9C, model M11) predicts slightly too low incision rates for some rivers (Estéron, Lower Tinée), but a good fit to $^{10}\text{Be}_{\text{MS}}$ and to some other rivers (Paillon and Roya), and rather high and constant $^{10}\text{Be}_{\text{MS}}$. Removing sea level changes does not significantly affect the simulated river incision rates, but gives a lower $^{10}\text{Be}_{\text{MS}}$ signal, with still an increase after -30 ka (Figure 9D, model M12). A simulation with constant precipitation rate gives satisfying results for the rivers incision rates but a constant and too low $^{10}\text{Be}_{\text{MS}}$, especially for the most recent (-20 to 0 ka) period (Figure 9E, model M13). Finally, removing both the flexural isostatic response of the lithosphere and the main sources of load (i.e., ice cover and sea level variations) has large effects both on the river incision rates (especially for the Vésubie River) and on the $^{10}\text{Be}_{\text{MS}}$ signal (Figures 9F and 9G, models M14 and M15). Interestingly, the last three models without precipitation changes, or without flexure +/- ice cover or sea level changes produce rather stable $^{10}\text{Be}_{\text{MS}}$ values throughout the model.

Based on these models, we show that:

- Simulation with constant precipitations or without flexure and without either ice cover or sea level changes do not produce the observed increase in $^{10}\text{Be}_{\text{MS}}$ after 30-40 ka.
- The large incision rate in the Vésubie River (compared to Bévéra, Roya, Estéron and Paillon) can only be explained by the effect of isostatic rebound, the latter being smaller in the simulations with no glaciers.
- Cosmic ray exposure (CRE) data on river-polished walls only do not allow to discriminate between constant (0.5 mm.yr⁻¹) or variable (0.3 then 0.7 mm.yr⁻¹) precipitation rates.
- However, a constant precipitation induces more important denudation in the earliest stages of the predicted evolution (compared to the reference simulation where precipitation rate is low), hence producing on average a lower $^{10}\text{Be}_{\text{MS}}$ at the end of the model.
- A combination of sea level changes, ice cover and lithospheric flexure provides a reasonable fit both to river incision rates and to measured $^{10}\text{Be}_{\text{MS}}$.

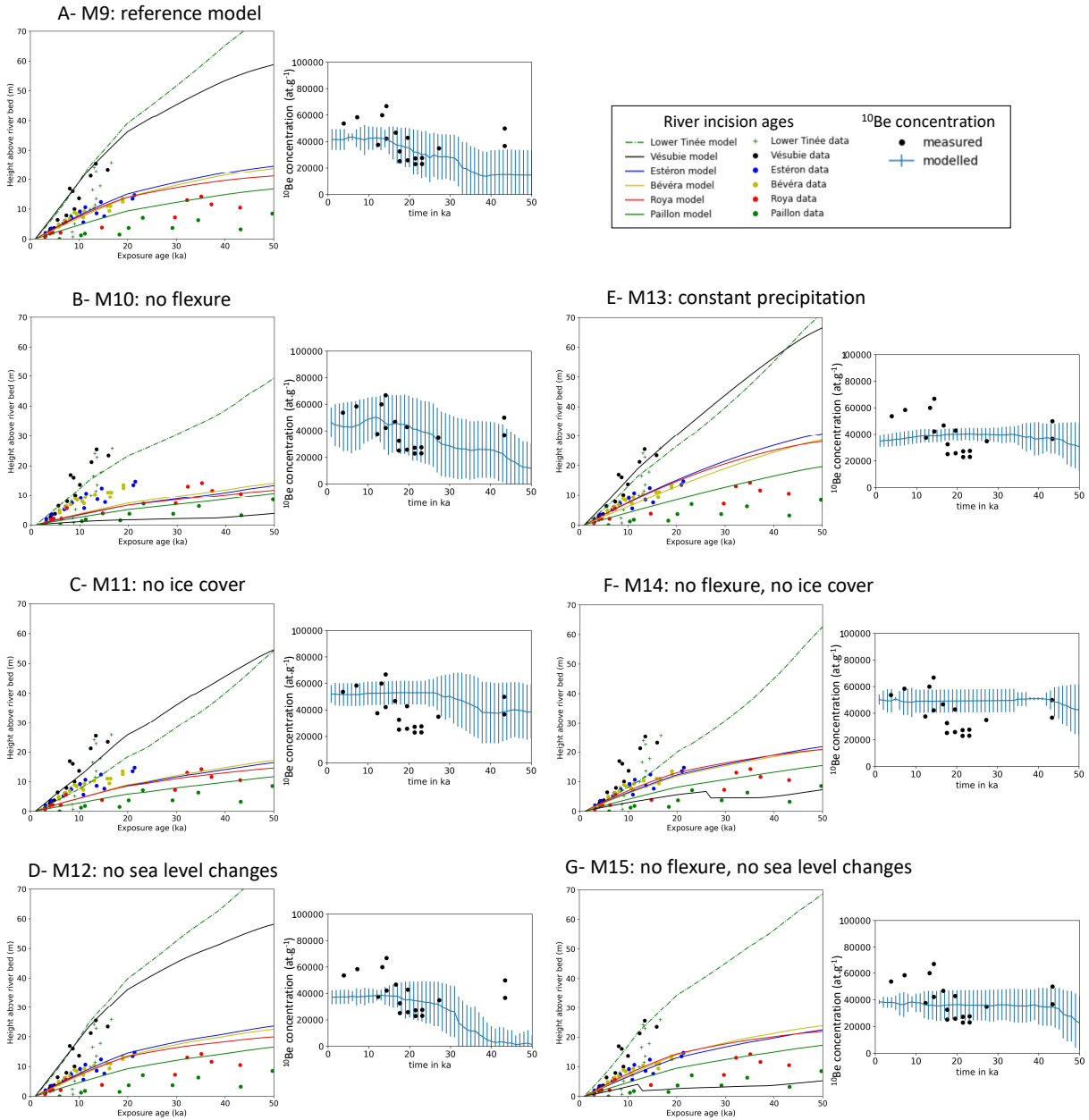


Figure 9. Comparison between model outputs and data from CRE ages in river-polished cliffs (left panels, see Figure 2) and $^{10}\text{Be}_{\text{MS}}$ (right panels, after Mariotti et al., 2021). Vertical bars on the right correspond to measured standard deviations in $^{10}\text{Be}_{\text{MS}}$ in the sampled area (Figure 8). See Table 3 for model parameters.

5 Discussion and Conclusions

These series of models, where continental sediment deposition is controlled almost exclusively by one parameter (the critical slope for alluvial deposition) show that it is sufficient to induce significant differences in the ^{10}Be signal between its production
385 in quartz-bearing rocks of high-altitude massifs and its record in the submarine domain. However, we do not capture here all the details of erosion, transport, sediment mixing and sedimentation, as we do not consider different lithologies, grain sizes, nor any complex mixing law between the various sediment sources. **Oppositely** to the study by Carretier et al. (2020), the lack of grain tracking prevents us from being able to measure particle residence times and confront them with the average geochemical signature of the sediments.

390 Submarine sediment transport and deposition modelling is almost as simple as on land, and does not consider ocean dynamics (turbulence of turbiditic flows, coastal currents), which are responsible for characteristic sedimentary features such as the Var sedimentary ridge at the bottom of the Var Canyon (Migeon et al., 2001). These phenomena can also contribute to sediment dispersion and smoothing of the ^{10}Be signal offshore.

Similarly, it could be interesting to couple our models with glacial erosion models (e.g., Seguinot and Delanay (2021)) in order
395 to better control the variability of glacial erosion and sediment production during the last cycles, and better quantify how it affects ^{10}Be production and exportation.

Finally, initial model conditions are another possible source of uncertainty, especially when it comes to our initial topography, which is derived from present-day elevation and therefore limits our ability to run the model over a longer period of times as it would produce a final topography too different from current one. A better estimate of initial quartz abundances in source rocks
400 (i.e., crystalline lithologies of the Mercantour massif and cenozoic sandstones of the foreland) would also help to reduce the uncertainties associated with quartz and ^{10}Be transfert from source to sink.

Our results based on dating and modelling indicate that, while river sands do accurately estimate the average denudation rate of continental catchments for the Var region (provided the latter does not vary at high frequency, i.e., with periods smaller than the time needed to reach steady-state), it is much less the case for submarine deep-sea sediments. These sediments have
405 a different, and often much smoother signature than continental ones, and record significant lag and/or relaxation times with respect to external forcing, probably due to the geomorphological response of the continental margin both on land and at sea. This area being prone to strong and rapid geomorphological modifications (i.e., transition from narrow bedrock channels to wide, braided rivers) during violent flood events (like during the Alex storm, which took place in October 2020), it could be of primordial importance to estimate the relaxation time of such events and their role on the long-term landscape evolution and
410 geochemical signature of the sedimentary archives.

On the long-term, the presence of ice in the massifs where ^{10}Be production occurs, together with the reworking of alluvial and deltaic sediments during low sea-level periods and vertical motions due to lithospheric flexure largely modify the signal coming from precipitation variations, and can lead to poor estimates of the actual denudation rate variations from $^{10}\text{Be}_{\text{MS}}$. All these effects have been exemplified in this study of the Var catchment where the distance from source to sink is short, precipitation
415 rates are large and the mouth of the main rivers are devoid of any large deltas. Hence, in regions with very large catchments,

alluvial plains and deltas, it could be even more difficult to reconstruct past denudation rates from deep sea sediments.

Our reference simulation highlights the complex interactions between river incision, sea level variations, ice coverage and the resulting isostatic response of the lithosphere. It seems impossible to disentangle the respective role of any of these forcing specifically, as most of them are interdependent. However, further tests (Figure 9) show that, depending on their location, 420 rivers have a different sensitivity to these parameters: the Estéron, Roya, Paillon and Bévéra are less affected by the parametric changes applied to the reference forcing conditions: their incision rate is only significantly reduced when considering no sea level changes, nor ice cover or flexure (not shown here).

Oppositely, the rivers with the largest incision rates (the Vésubie, and to a lesser extent, the Tinée River) are also the ones which seem more sensitive to the effect of ice cover and flexural isostatic response of the lithosphere (Figure 9). It is possibly 425 because a significant part of their length (20-40) runs over the Mercantour crystalline massif, i.e. over the area where post-glacial isostatic rebound is important. The sampling sites of these rivers being rather close to their headwaters, they are not sensitive to sea level variations. Quantification of each river sensitivity to local or regional processes like isostatic uplift, sea level changes, precipitation or ice cover, depending on the dating site location, could therefore be useful to better understand the respective importance of these external forcing on this South Alpine margin.

430 *Code and data availability.* The corresponding version of Badlands with all the data used for this paper can be found here: <https://github.com/badlands-model/badlands-Be>

Author contributions. CP developed the implementation for Badlands, performed model runs and redaction; TS checked and released the new version of the code and participated to the redaction. YR, VG and LA participated to the redaction.

Competing interests. The authors declare no conflict of interest.

435 *Acknowledgements.* This study is part of a project that has been funded by the French Geological Survey (Bureau de Recherches Géologiques et Minières; BRGM) through the national program “Référentiel Géologique de France” (RGF-Alpes). This work has been supported by the French government, through the UCA-JEDI Investments in the Future project managed by the National Research Agency (ANR) with the reference number ANR-15-IDEX-01. Fruitful discussions with Guillaume Duclaux (Geoazur) were greatly appreciated. The authors thank 440 Sebastien Carretier and Yanyan Wang for their insightful comments on the first version of this manuscript, and to Associate Editor Simon Mudd for handling the review process.

References

- Armitage, J., Dunkley Jones, T., Duller, R., Whittaker, A., and Allen, P.: Temporal buffering of climate-driven sediments flux cycles by transient catchment response, *Earth and Planetary Science Letters*, 369-370, 200–210, <https://doi.org/10.1016/j.epsl.2013.03.020>, 2013.
- Audra, P., Mocochain, L., Bigot, J.-Y., and D'Antoni-Noblecourt, J.-C.: The Grand Coyer karst, exploration at the Coulomp spring (Alpes-de-Haute-Provence, France, Proceedings of the 15th International Congress of Speleology, pp. 1755–1759, 2009.
- 445 Bentley, S., Blum, M., Maloney, J., Pond, L., and Paulsell, R.: The Mississippi River source-to-sink system: Perspectives on tectonic, climatic, and anthropogenic influences, Miocene to Anthropocene, *Earth-Science Reviews*, 153, 139–174, <https://doi.org/10.1016/j.earthscirev.2015.11.001>, 2016.
- Bierman, P. and Steig, E.: Estimating Rates of Denudation Using Cosmogenic Isotope Abundances in Sediment, *Earth Surface Processes and Landforms*, 21, 125–139, 1996.
- 450 Blöthe, J. and Korup, O.: Millennial lag times in the Himalayan sediment routing system, *Earth and Planetary Science Letters*, 382, 38–46, <https://doi.org/10.1016/j.epsl.2013.08.044>, 2013.
- Bonneau, L., Toucanne, S., Bayon, G., Jorry, S., Emmanuel, L., and Silva Jacinto, R.: Glacial erosion dynamics in a small mountainous watershed (Southern French Alps): A source-to-sink approach, *Earth and Planetary Science Letters*, 458, 366–379, <https://doi.org/10.1016/j.epsl.2016.11.004>, 2016.
- 455 Boulton, G.: Theory of glacial erosion, transport and deposition as a consequence of subglacial sediment deformation, *Journal of Glaciology*, 42, 43–62, <https://doi.org/10.3189/S0022143000030525>, 1996.
- Braucher, R., Merchel, S., Borgomano, J., and Bourlès, D.: Production of cosmogenic radionuclides at great depth : A multi element approach, *Earth and Planetary Science Letters*, 309, 1–9, <https://doi.org/10.1016/j.epsl.2011.06.036>, 2011.
- 460 Brisset, E., Guiter, F., Miramont, C., Revel, M., Anthony, E., Delhon, Arnaud, F., E., E. M., and de Beaulieu, J.-L.: Lateglacial/Holocene environmental changes in the Mediterranean Alps inferred from lacustrine sediments, *Quaternary Science Reviews*, 110, 49–71, <https://doi.org/10.1016/j.quascirev.2014.12.004>, 2015.
- Burov, E. and Diament, M.: The effective elastic thickness T_e of continental lithosphere What does it really mean, *Journal of Geophysical Research*, 100, 3905–3297, 1995.
- 465 Cardinal, T., Rolland, Y., Petit, C., Audin, L., Zerathe, S., Schwartz, S., and the ASTER Team: Fluvial bedrock gorges as markers for Late-Quaternary tectonic and climatic forcing in the French Southwestern Alps, *Geomorphology*, submitted, <https://doi.org/10.1016/j.earthscirev.2021.103809>, 2022.
- Carretier, S., Regard, V., Vassallo, R., Martinod, J., Christophoul, F., Gayer, E., Audin, L., and Lagane, C.: A note on ^{10}Be -derived mean erosion rates in catchments with heterogeneous lithology: examples from the western Central Andes, *Earth Surface Processes and Landforms*, 40, 1719–1729, <https://doi.org/https://doi.org/10.1002/esp.3748>, 2015.
- 470 Carretier, S., Guerit, L., Harries, L., Regard, V., Maffre, P., and Bonnet, S.: The distribution of sediment residence times at the foot of mountains and its implications for proxies recorded in sedimentary basins, *Earth and Planetary Science Letters*, <https://doi.org/10.1016/j.epsl.2020.116448>, 2020.
- Clift, P. and Giosan, L.: Sediment fluxes and buffering in the post-glacial Indus Basin, *Basin Research*, 26, 369–386, <https://doi.org/10.1111/bre.12038>, 2014.
- 475 Codilean, A., Bishop, P., Hoey, T., Stuart, F., and Fabel, D.: Cosmogenic ^{21}Ne analysis of individual detrital grains: opportunities and limitations, *Earth Surface Processes and Landforms*, 35, 16–27, <https://doi.org/10.1002/esp.1815>, 2010.

- Fryirs, K., Brierley, G., Preston, N., and Kasai, M.: Buffers, barriers and blankets: The (dis)connectivity of catchment-scale sediment cascades, *Catena*, 70, 49–67, <https://doi.org/10.1016/j.catena.2006.07.007>, 2007.
- 480 Godard, V. and Tucker, G.: Influence of Climate-Forcing Frequency on Hillslope Response, *Geophysical Research Letters*, 48, e2021GL094305, <https://doi.org/https://doi.org/10.1029/2021GL094305>, 2021.
- Goren, L.: A theoretical model for fluvial channel response time during time-dependent climatic and tectonic forcing and its inverse applications, *Geophysical Research Letters*, 43, 10,753–10,763, <https://doi.org/10.1002/2016GL070451>, 2016.
- Hayes, A., Kucera, M., Kallel, N., Sbaffi, L., and Rohling, E.: Lateglacial/Holocene environmental changes in the Mediterranean Alps
485 inferred from lacustrine sediments, *Quaternary Science Reviews*, 110, 49–71, <https://doi.org/10.1016/j.quascirev.2014.12.004>, 2015.
- Jerolmack, D. and Paola, C.: Shredding of environmental signals by sediment transport, *Geophysical Research Letters*, 37, <https://doi.org/https://doi.org/10.1029/2010GL044638>, 2010.
- Knudsen, M., Egholm, D., and Jansen, J.: Time-integrating cosmogenic nuclide inventories under the influence of variable erosion, exposure, and sediment mixing, *Quaternary Geochronology*, 51, 110–119, <https://doi.org/10.1016/j.quageo.2019.02.005>, 2019.
- 490 Lal, D.: Cosmic ray labeling of erosion surfaces: in situ nuclide production rates and erosion models, *Earth and Planetary Science Letters*, 104, 424–439, 1991.
- Li, C., Yang, S., Zhao, J., Xin, J., Dosseto, A., Bi, L., and Clark, T.: The time scale of river sediment source-to-sink processes in East Asia, *Chemical Geology*, 446, 138–146, <https://doi.org/10.1016/j.chemgeo.2016.06.012>, 2016.
- Liu, Z., Zhao, Y., Colin, C., Statterger, K., Wiesner, M., Huh, C., and Li, Y.: Source-to-sink transport processes of fluvial sediments in the
495 South China Sea, *Earth-Science Reviews*, 153, 238–273, <https://doi.org/10.1016/j.earthscirev.2015.08.005>, 2016.
- Lupker, M., Blard, P.-H., Lavé, J., France-Lanord, C., Leanni, L., Puchol, N., Charreau, J., and Bourlès, D.: ^{10}Be -derived Himalayan denudation rates and sediment budgets in the Ganga basin, *Earth and Planetary Science Letters*, 333-334, 146–156, <https://doi.org/10.1016/j.epsl.2012.04.020>, 2012.
- Malatesta, L., Avouac, J.-P., Brown, N., Breitenbach, S., Pan, J., Chevalier, M., Rhodes, E., Saint-Carlier, D., Zhang, W., Charreau, J., Lavé, J.,
500 and Blard, P.-H.: Lag and mixing during sediment transfer across the Tian Shan piedmont caused by climate-driven aggradation–incision cycles, *Basin Research*, 30, 613–635, <https://doi.org/10.1111/j.bre.12267>, 2018.
- Mandal, S., Lupker, M., Burg, J.-P., Valla, P., Haghpor, N., and Christl, M.: Spatial variability of ^{10}Be -derived erosion rates across the southern Peninsular Indian escarpment: A key to landscape evolution across passive margins, *Earth and Planetary Science Letters*, 425, 154–167, <https://doi.org/10.1016/j.epsl.2015.05.050>, 2015.
- 505 Mariotti, A., Blard, P.-H., Charreau, J., Petit, C., and Molliex, S.: Denudation systematics inferred from in situ cosmogenic ^{10}Be concentrations in fine (50-100 μm) and medium (100-250 μm) sediments of the Var River basin, southern French Alps, *Earth Surface Dynamics*, 7, 1059–1074, <https://doi.org/10.5194/esurf-7-1059-2019>, 2019.
- Mariotti, A., Blard, P.-H., Charreau, J., Toucanne, S., Jorry, S., Molliex, S., and Keddadouche, K.: Nonlinear forcing of climate on mountain denudation during glaciations, *Nature Geoscience*, 14, 16–22, <https://doi.org/10.1038/s41561-020-00672-2>, 2021.
- 510 Martin, L., Blard, P.-H., Balco, G., Lavé, J., Delunel, R., Lifton, N., and Laurent, V.: The CREp program and the ICE-D production rate calibration database: A fully parameterizable and updated online tool to compute cosmic-ray exposure ages, *Quaternary Geochronology*, 38, 25–49, <https://doi.org/https://doi.org/10.1016/j.quageo.2016.11.006>, 2017.
- Migeon, S., Savoye, B., Zanella, E., Mulder, T., Faugères, J.-C., and Weber, O.: Detailed seismic-reflection and sedimentary study of turbidite sediment waves on the Var Sedimentary Ridge (SE France): significance for sediment transport and deposition and for the mechanisms of
515 sediment-wave construction, *Marine and Petroleum Geology*, 18, 179–208, 2001.

- Mulder, T., Savoye, B., Piper, D., and Syvitski, J.: The Var submarine sedimentary system: understanding Holocene sediment delivery processes and their importance to the geological record, *Geological Society of London Special Publications*, 129, 146–166, 1998.
- Norton, K. and Vanacker, V.: Effects of terrain smoothing on topographic shielding correction factors for cosmogenic nuclide-derived estimates of basin-averaged denudation rates, *Earth Surface Processes and Landforms*, 34, 145–154, <https://doi.org/10.1002/j.esp.1700>, 2009.
- 520 Petit, C., Migeon, S., and Coste, M.: Numerical models of continental and submarine erosion: Application to the northern Ligurian Margin, *Earth Surface Processes and Landforms*, 425, 681–695, <https://doi.org/10.1002/j.esp.3685>, 2015.
- Petit, C., Goren, L., Rolland, Y., Bourlès, D., Braucher, R., Saillard, M., and Cassol, D.: Recent, climate-driven river incision rate fluctuations in the Mercantour crystalline massif, southern French Alps, *Quaternary Science Reviews*, 165, 73–87, <https://doi.org/10.1016/j.quascirev.2017.04.015>, 2017.
- 525 Petit, C., Rolland, Y., Braucher, R., Bourlès, D., Guillou, V., and PetitPerrin, V.: River incision and migration deduced from ^{36}Cl cosmic-ray exposure durations: The Clue de la Cerise gorge in southern French Alps, *Geomorphology*, 330, 81–88, <https://doi.org/10.1016/j.geomorph.2019.01.011>, 2019.
- Phillips, J. and Slattery, M.: Sediment storage, sea level, and sediment delivery to the ocean by coastal plain rivers, *Progress in Physical Geography*, 30, 513–530, <https://doi.org/10.1191/0309133306pp494ra>, 2006.
- 530 Repka, J., Anderson, R., and Finkel, R.: Cosmogenic dating of fluvial terraces, Fremont River, Utah, *Earth and Planetary Science Letters*, 152, 59–73, 1997.
- Rodrigo-Gamiz, M., Martinez-Ruiz, F., Rampen, S., Schouten, S., and Sinninghe Damsté, J.: Sea surface temperature variations in the western Mediterranean Sea over the last 20 kyr: A dual-organic proxy, *Paleoceanography*, 29, 87–98, <https://doi.org/10.1002/2013PA002466>, 2013.
- Rolland, T., Darnault, R., Braucher, R., Bourlès, D., Petit, C., and Bouissou, S.: Deglaciation history at the Alpine-Mediterranean transition (Argentera-Mercantour, SW Alps) from ^{10}Be dating of moraines and glacially polished bedrock, *Earth Surface Processes and Landforms*, 45, 393–410, <https://doi.org/10.1002/esp.4740>, 2020.
- 535 Rolland, Y., Petit, C., Saillard, M., Braucher, R., Bourlès, D., Darnault, R., and Cassol, D.: Inner gorges incision history: A proxy for deglaciation? Insights from Cosmic Ray Exposure dating (^{10}Be and ^{36}Cl) of river-polished surfaces (Tinée River, SW Alps, France), *Earth and Planetary Science Letters*, 457, 271–281, <https://doi.org/10.1016/j.epsl.2016.10.007>, 2017.
- 540 Romans, B., Castellort, S., Covault, J., Fildani, A., and Walsh, J.: Environmental signal propagation in sedimentary systems across timescales, *Earth-Science Reviews*, 153, 7–29, <https://doi.org/10.1016/j.earthscrev.2015.07.012>, 2016.
- Saillard, M., Petit, C., Rolland, Y., Braucher, R., Bourlès, D., Zerathe, S., and Jourdon, A.: Late Quaternary incision rates in the Vésubie catchment area (Southern French Alps) from in situ-produced ^{36}Cl cosmogenic nuclide dating: Tectonic and climatic implications, *Journal of Geophysical Research: Earth Surface*, 119, 1121–1135, <https://doi.org/10.1002/2013JF002985>, 2014.
- 545 Salles, T.: Badlands : A parallel basin and landscape dynamics model, *SoftwareX*, 5, 195–202, <https://doi.org/10.1016/j.softx.2016.08.005>, 2016.
- Seguinot, J. and Delanay, I.: Last-glacial-cycle glacier erosion potential in the Alps, *Earth Surface Dynamics*, 9, 923–935, <https://doi.org/10.5194/esurf-9-923-2021>, 2021.
- Siame, L., Angelier, J., Godard, R. C. V., Derrieux, F., Bourlès, D., Braucher, R., Chang, K.-J., Chu, H.-T., and Lee, J.-C.: Erosion rates in an active orogen (NE-Taiwan): A confrontation of cosmogenic measurements with river suspended loads, *Quaternary Geochronology*, 6, 246–260, <https://doi.org/10.1016/j.quageo.2010.11.003>, 2011.
- Syvitski, J., Morehead, M., Bahr, D., and Mulder, T.: Estimating fluvial sediment transport : The rating parameters, *Water Resources*, 36, 2747–2760, 2000.

- Syvitski, J., Angel, J., Saito, Y., Overeem, I., Vörösmarty, C., Wang, H., and Olago, D.: Earth's sediment cycle during the Anthropocene, *Nature Review Earth and Environment*, 3, 179–196, <https://doi.org/10.1038/s43017-021-00253-w>, 2022.
- 555 Thran, A., East, M., Webster, J., Salles, T., and Petit, C.: The influence of carbonate platforms on the geomorphological development of a mixed carbonate-siliciclastic margin (Great Barrier Reef, Australia), *Geochemistry, Geophysics, Geosystems*, 21, <https://doi.org/10.1029/2020GC008915>, 2020.
- Vanacker, V., von Blanckenburg, F., Hewawasam, T., and Kubik, P.: Constraining landscape development of the Sri Lankan escarpment with cosmogenic nuclides in river sediment, *Earth and Planetary Science Letters*, 253, 402–414, <https://doi.org/10.1016/j.epsl.2006.11.003>, 2007.
- 560 von Blanckenburg, F.: The control mechanisms of erosion and weathering at basin scale from cosmogenic nuclides in river sediment, *Earth and Planetary Science Letters*, 237, 462–479, <https://doi.org/10.1016/j.epsl.2005.06.030>, 2005.
- Waelbroeck, C., Labeyrie, L., Michel, L., Duplessy, J., McManus, J., Lambeck, K., Balbon, E., and Labracherie, M.: Sea-level and deep water temperature changes derived from benthic foraminifera isotopic records, *Quaternary Science Reviews*, 21, 295–305, [https://doi.org/10.1016/S0277-3791\(01\)00101-9](https://doi.org/10.1016/S0277-3791(01)00101-9), 2002.
- 565 Wan, S., Li, A., Clift, P., and Jiang, H.: Development of the East Asian summer monsoon: Evidence from the sediment record in the South China Sea since 8.5 Ma, *Palaeogeography, Palaeoclimatology, Palaeoecology*, 241, 139–159, <https://doi.org/10.1016/j.palaeo.2006.06.013>, 2006.
- 570 Whipple, K. and Tucker, G.: Dynamics of the stream-power river incision model: Implications for height limits of mountain ranges, landscape response timescales, and research needs, *Journal of Geophysical Research*, 104, 17,661–17,674, 1999.
- Wickert, A.: Open-source modular solutions for flexural isostasy: gFlex v1.0, *Geoscientific Model Development*, 9, 997–1017, <https://doi.org/10.5194/gmd-9-997-2016>, 2016.
- Yanites, B., Tucker, G., and Anderson, R.: Numerical and analytical models of cosmogenic radionuclide dynamics in landslide-dominated drainage basins, *Journal of Geophysical Research*, 114, F01 007, <https://doi.org/10.1029/2008JF001088>, 2009.
- 575 Zerathe, S., Litty, C., Blard, P.-H., Delgado, F., Audin, L., and Carcaillet, J.: Cosmogenic ³He and ¹⁰Be denudation rates in the Central Andes: Comparison with a natural sediment trap over the last 18 ka, *Earth and Planetary Science Letters*, 599, 117 869, <https://doi.org/https://doi.org/10.1016/j.epsl.2022.117869>, 2022.